Chapter 2
Effect of Induced Porosity on Fatigue Performance of Additively Manufactured Short-Fiber Thermoplastics Using Infrared Thermography

Harsh Gandhi, Pharindra Pathak, and Suhasini Gururaja

Abstract This study explores the influence of induced porosity on the fatigue behavior of additively manufactured short-fiber thermoplastics (AM-SFTs), employing infrared thermography (IRT) as an accelerated characterization method. IRT has emerged as a validated technique for drastically reducing the time required to estimate fatigue limits, offering a more efficient alternative to the conventional stress-life (S-N) method. In a previous study, acquiring the S-N curve for 20% short carbon fiber-reinforced Acrylonitrile Butadiene Styrene (CF/ABS) panels required two weeks of testing with 18 specimens. IRT testing achieved comparable fatigue limit estimates using only three specimens over five hours. This underscores the effectiveness of IRT in providing rapid fatigue assessments [1]. In this research, specimens composed of 80% ABS and 20% chopped carbon fibers were produced via fused deposition modeling (FDM) and subjected to fatigue loading. The study considered 16-layer AM-SFT specimens with artificially induced discrete porosity - 6 mm diameter defects located on the middle layer of the specimen. Additionally, control specimens with no pores have also been tested. A test matrix of 15 specimens consistent with ASTM D638 Type I specifications, with five replicates per configuration, has been tested. Each specimen was tested under both static and cyclic loading conditions. IRT facilitated real-time monitoring of surface temperature changes during fatigue testing, a precursor to fatigue damage initiation. This investigation aims to establish a quantitative relationship between defect size, location, and fatigue performance in AM-SFTs. The findings will provide deeper insights into the role of porosity in fatigue behavior and offer more efficient methodologies for fatigue characterization in AM composites.

Keywords Fatigue limit · Engineered defects · AM-SFTs · IRT · Damage

Introduction

Additive manufacturing has revolutionized material design and production, particularly with its ability to fabricate lightweight, high-performance components with tailored properties [2]. Among the most promising materials in this field are additively manufactured short-fiber thermoplastics, which combine polymer matrices with reinforcing short fibers to achieve improved mechanical properties [2]. These materials are commonly produced using fused deposition modeling, a process that offers manufacturing flexibility but can introduce defects, such as porosity, which significantly impact structural integrity under cyclic loading [1, 3].

Porosity in AM components is a critical concern as it acts as a stress concentrator, promoting damage initiation and propagation, thereby accelerating fatigue failure [4]. Fatigue damage, which progressively accumulates in materials under cyclic loading, can substantially affect the residual stiffness and strength of SFTs. Gaining insight into this damage and its influence on material properties is crucial for accurately predicting the lifespan and structural integrity of SFT-based components [1]. Traditional fatigue characterization using stress-life testing is time-consuming and resource-intensive, requiring numerous specimens and long test durations [5]. To address these challenges, infrared thermography has emerged as an effective alternative, offering rapid, real-time monitoring of damage accumulation by detecting thermal responses during cyclic loading [6, 7].

Harsh Gandhi · Pharindra Pathak · Suhasini Gururaja
Department of Aerospace Engineering, Auburn University, Auburn, AL 36849
e-mail: hsg0014@auburn.edu; pzp0057@auburn.edu; suhasini.gururaja@auburn.edu

Garrett Pataky et al. (eds.), *Fracture, Fatigue, Failure, Damage Evolution and Thermomechanics & Infrared Imaging, Vol. 4*,
Conference Proceedings of the Society for Experimental Mechanics Series, https://doi.org/10.13052/97887-438-0830-5_2

This study investigates the effect of engineered defects on the fatigue behavior of AM-SFTs. The specimens, composed of CF/ABS, were fabricated using FDM with ±45° fiber orientations following the ASTM D638 Type I standard. Engineered defects of 6 mm diameter were introduced in the 8th layer (middle layer) of select specimens to study the influence of porosity on fatigue performance. A total of 15 specimens were tested under static and fatigue loading conditions and monitored using IRT to capture temperature variations corresponding to fatigue damage initiation.

Background

Materials

To investigate the fatigue performance of AM-SFTs with varying defect configurations, a detailed test matrix was developed, as shown in **Table. 1**. The specimens, fabricated according to ASTM D638 Type I standards, were composed of 20% chopped carbon fibers and 80% ABS. The samples were printed using a fused deposition modeling (FDM) process with a 0.4 mm nozzle diameter and a printing temperature of 240°C. A rectilinear infill pattern with 100% sparse infill density was utilized to ensure consistent material properties throughout the specimens. The fine print setting was selected to improve dimensional accuracy and surface quality. The total printing duration for each specimen was approximately 20 min per specimen. The ±45° fiber orientation was chosen to mitigate shear failure observed in previous tests with 0° laminates, which exhibited premature failure due to shear-dominated loading. This orientation helps distribute the load more effectively across the matrix, improving structural integrity during cyclic loading.

Table 1 Test Matrix for 3D Printed Specimens

Specimen	Material	Fiber aspect ratio (L / D)	3D Printer	% Infill	Ratio $\left(\frac{\sigma_{min}}{\sigma_{max}}\right)$	Frequency (Hz)	Nozzle Dia (mm)
ASTM D638 Type I	80 wt.% ABS 20 wt.% Carbon Fiber	5-8	Bambu Lab X1 Carbon	100	0.1	15	0.4
Configuration	**Specimen ID**	**Orientation (deg)**	**Defect Layer**	**No. of Replicates**	**Specimen Printed**	**Testing**	**Testing Completed**
Pristine	PRIS-STC-ALT45-#	±45	N/A	5	5	Static	5
Pristine	PRIS-FTG-ALT45-#	±45	N/A	5	5	Fatigue	5
6 mm Dia on Middle/8th Layer	6D-8L-FTG-ALT45-#	±45	8th	5	5	Fatigue	5
Total Specimens				**15**	**15**		**15**

The ASTM D638 Type I geometry was chosen due to its widespread use in tensile and fatigue testing of polymeric materials, providing reproducible and reliable mechanical property assessments [7]. The specimen geometry, depicted in **Fig. 1**, included a gauge section measuring 57 mm in length and 13 mm in width, with a thickness of 3.2 mm. Each

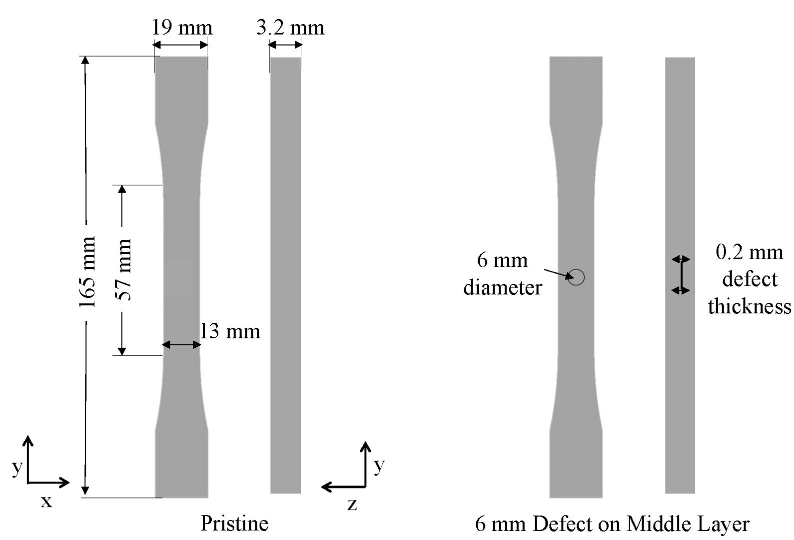

Fig. 1 ASTM D638 Type I Standard Specimen containing 20% CF and 80% ABS materials: pristine specimen (left), defect specimen (right)

specimen consists of 16 layers (0.2 mm thick) additively manufactured on top of each other. As shown in **Table. 1**, two sets of specimens were printed: Pristine specimens and specimens with 'engineered' defects. Engineered defect specimens comprised a 6 mm diameter pore region that was not printed, strategically placed on the 8^{th} (middle) layer.

IRT Testing Procedure

All tests, static tensile and fatigue tests were conducted using an MTS Landmark servohydraulic universal test frame with a 100 kN capacity, as shown in **Fig. 2**. Quasi-static tensile tests were performed at a 2 mm/min displacement-controlled rate to determine the mechanical properties—stiffness and ultimate tensile strength of the CF/ABS composite specimen. Gage pressure was kept around 325 psi to prevent specimen slippage. The strain was measured using an extensometer with a 5 cm gauge length. Five specimens were tested, yielding an average ultimate tensile strength (σ_{uts}) of 27.00 ± 1.49 MPa, failure strain (ϵ_f) of $4.66\% \pm 0.46\%$, and an elastic modulus (E_0) of 2.02 ± 0.16 GPa, which served as the baseline for subsequent fatigue testing.

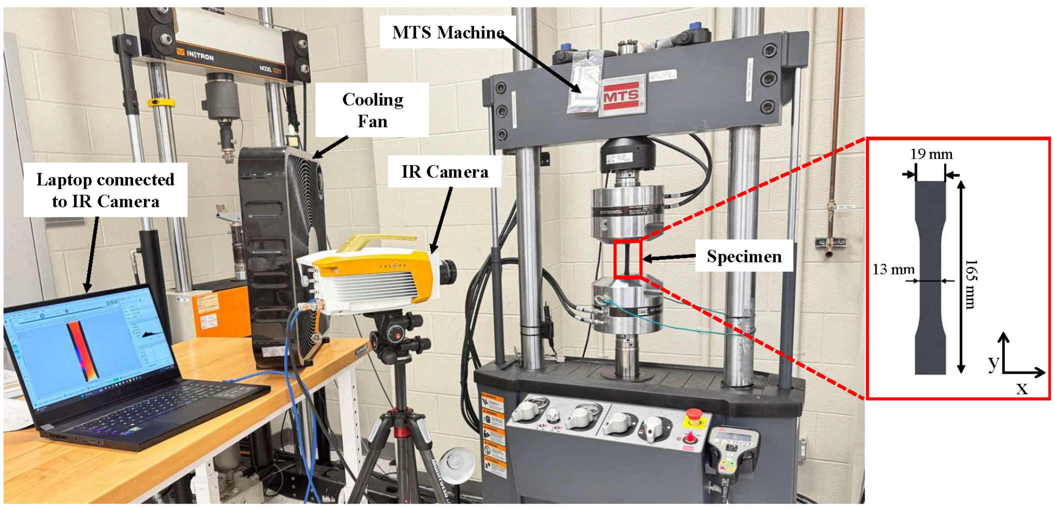

Fig. 2 Experimental Setup for Fatigue Testing

Tension-tension fatigue tests were conducted under sinusoidal load-controlled conditions with a stress ratio $R = 0.1$. The maximum and minimum loads were set as percentages of the average σ_{uts}. The loading frequency was maintained at 15 Hz, following the approach in [8, 9, 10]. **Fig. 3** illustrates the staircase cyclic loading with $R = 0.1$. Temperature

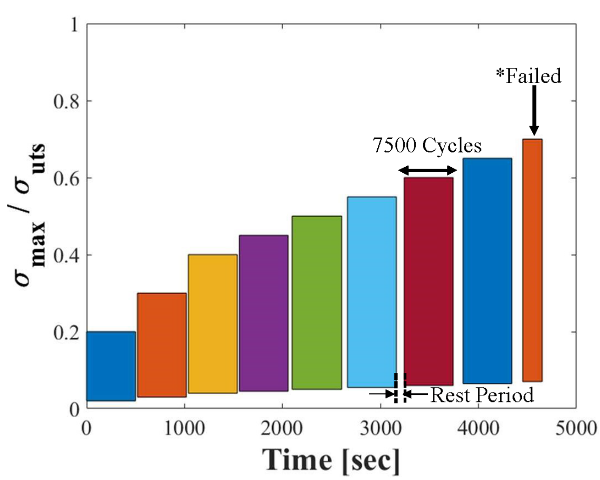

Fig. 3 Staircase loading applied to a specimen to determine fatigue limit rapidly with an early increment of 10% σ_{uts} followed by 5% σ_{uts} increments to σ_{max}. The stress ratio R = 0.1 was maintained throughout the test. The rest period between load steps ensured the specimen cooled down to room temperature after every step load

measurements were obtained in real-time using a Telops Spark M150 MWIR cooled camera (640 × 512 pixels, 20 mK NETD, 3-5.4 μm spectral range) at a data acquisition frequency of 100 Hz. Data acquisition was done via Reveal IR software, and surface temperature evolution was analyzed to identify fatigue limits and correlate them with defect location and fatigue performance. The fatigue limit was determined by plotting the stabilization temperature change (ΔT_{stab}) for each step ($\sigma_{\max}$). The intersection of bi-linear curves fitting the ΔT_{stab} versus $\sigma_{\max}$ data marked the fatigue onset point, identified by the most significant change in slope. The step size (N_{step}) was fixed at 7500 cycles, based on trial tests, to establish the Phase II stabilized steady-state zone. A minimum of five replicates were tested for reliability. Fatigue testing was paused after each load step to allow cooling to room temperature before the next step. The cooling phase called the 'rest period' in **Fig. 3**, ensured specimens started each load step at ambient temperature. Following each rest period, a static test was performed to assess stiffness degradation as a function of load cycles.

Results and Discussion

The fatigue behavior of both pristine and defected specimens was examined through IRT during cyclic loading at increasing stress levels, as shown in **Fig. 4a - 4b**. The pristine specimen displayed minimal temperature variations across all stress levels, with only slight increases at 60% and 65% of the ultimate tensile strength (UTS), indicating a more uniform stress distribution and a delayed onset of internal damage (see **Fig. 4a**). In contrast, the specimen with a 6 mm diameter defect in the middle layer showed notable localized heating at higher stress levels (55%, 60%, and 65% of UTS) (see **Fig. 4b**). The localized heating observed in the engineered defect specimen suggests stress concentrations around the engineered defect, highlighting the role of porosity in accelerating fatigue damage. However, the overall temperature for both pristine and engineered defect specimens remained almost constant, with the defect specimen showing more localized heating due to stress concentration at higher loading levels.

Despite the observed thermal variations, the fatigue limit of the defected specimen, determined through a bilinear plot, was 49.52% ± 0.99% UTS (see **Fig. 5a - 5b**), which was only marginally higher than the pristine specimen's fatigue limit of 49.04% ± 1.28% UTS (see **Fig. 6a - 6b**). This suggests that the defect did not drastically reduce the fatigue resistance as initially expected.

Several factors contributed to this unexpected outcome. Firstly, the MTS machine used in the testing had a load capacity of 100 kN. Since the failure load of the tested specimens was around 1.08 kN, the applied loads were lower than

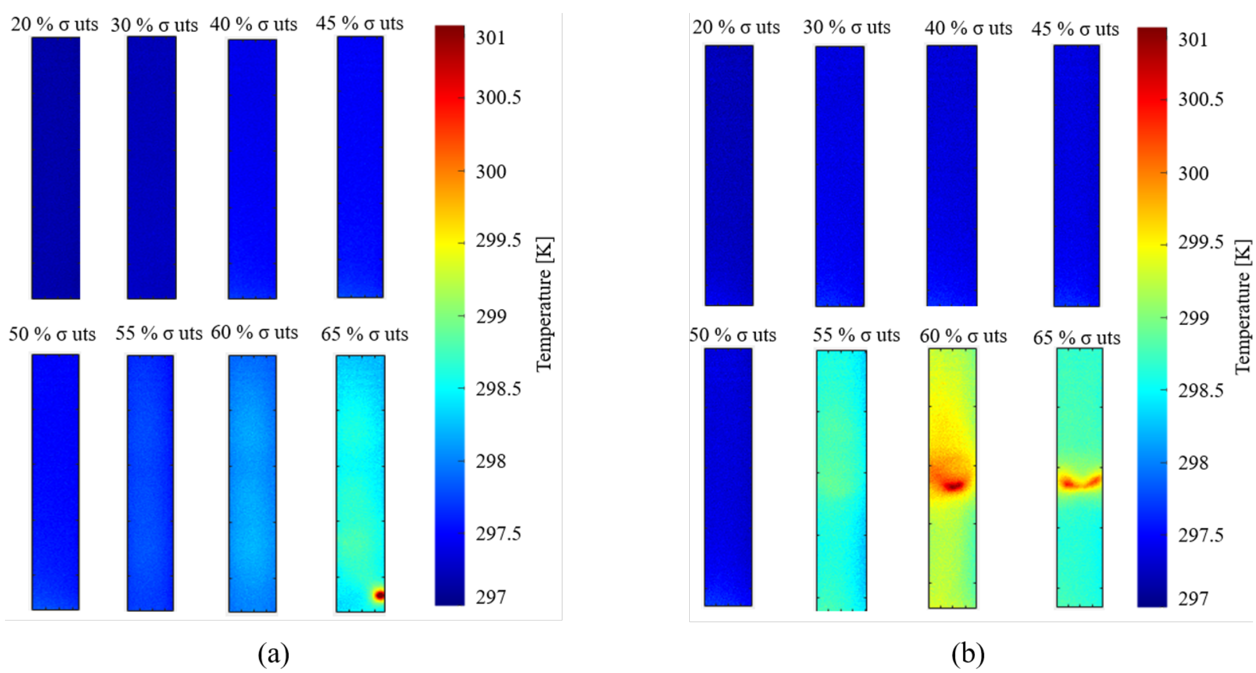

Fig. 4 Temperature displayed within the region of interest for each step loading for both (a) Pristine and (b) Engineered Defect Specimens

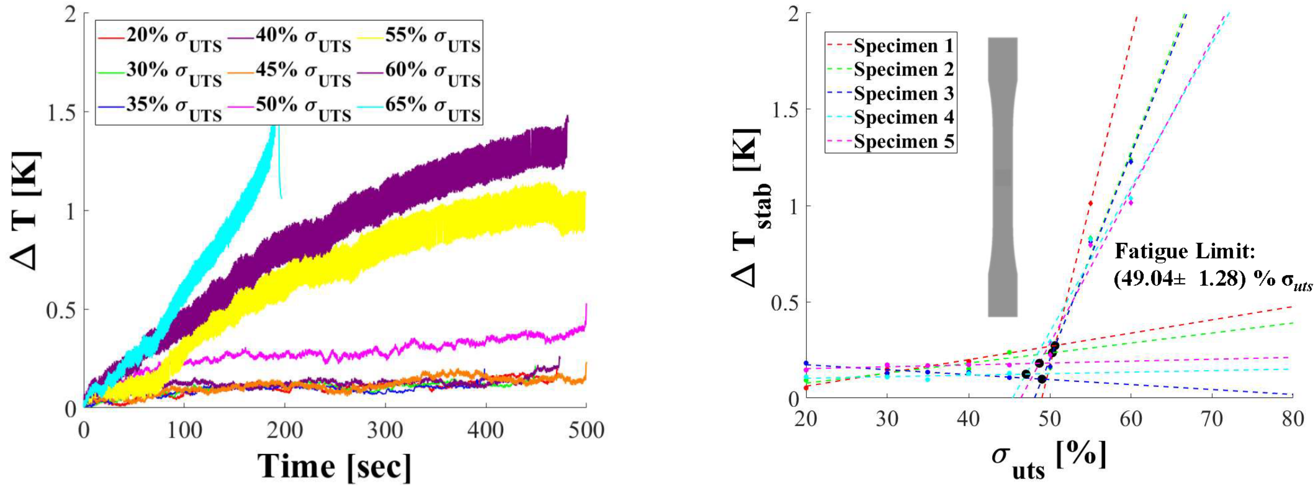

(a) (b)

Fig. 5 For Pristine, (a) Temperature vs. Time plot showing the temperature rise for Specimen 4 and (b) Fatigue Limit calculated from the Bilinear Plot for all the specimen

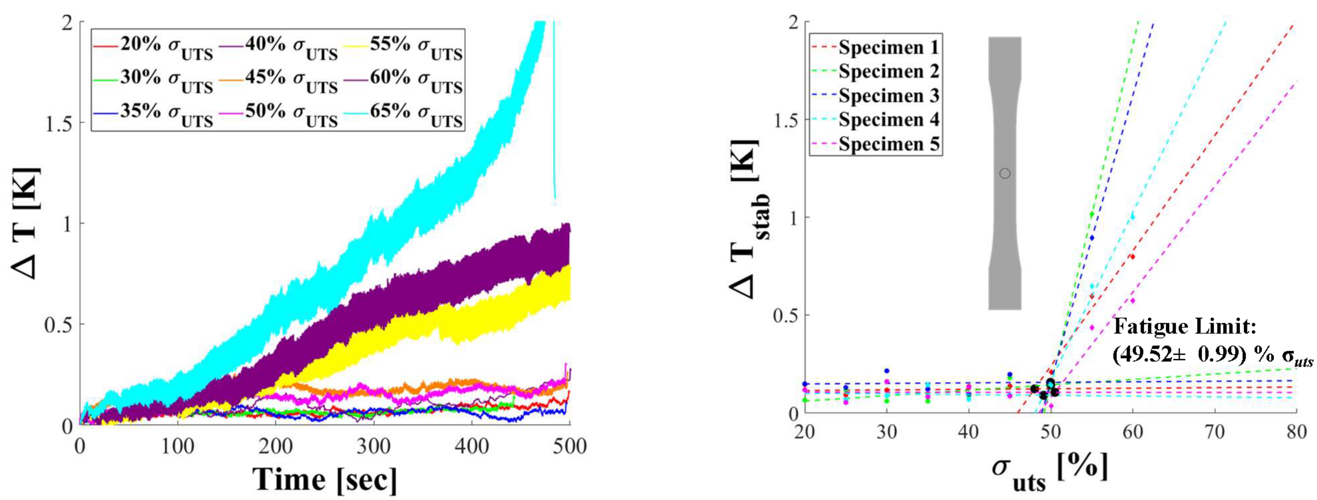

(a) (b)

Fig. 6 For 6mm diameter defect on the middle layer, (a) Temperature vs. Time plot showing the temperature rise for Specimen 2 and (b) Fatigue Limit calculated from the Bilinear Plot for all the specimen

the resolution of the MTS machine, potentially affecting the accuracy of the applied load. Secondly, although the engineered defect was intended to be placed in the middle layer (the 8th layer out of 16), micro-CT imaging revealed discrepancies in the actual defect size and shape. The analysis showed that the CF/ABS deposited filament over the defect location, effectively eliminating the void. This indicated that material consolidation during printing contributed to partially filling the defect (see **Fig. 7**), altering its intended geometry, and reducing its influence on fatigue performance. Additionally, due to the defect's depth within the specimen, the thermal signals detected by the infrared camera might have been lower, limiting the ability to capture conclusive temperature data at lower stress levels. This, combined with the resolution constraints of the MTS machine, may have contributed to the inconclusive temperature readings observed at lower load levels. Although localized heating was observed at 55-65% UTS, corresponding to the onset of fatigue damage around the defect, further investigation is needed to determine the defect's true impact on damage initiation at lower stress levels.

In summary, while the presence of the defect was expected to reduce the specimen's fatigue performance due to stress concentration, the results indicate that the fatigue resistance of the defected specimen was comparable to the pristine

Fig. 7 Microstructure of engineered defect specimen at 0.6 microns voxel size

specimen. This finding emphasizes the influence of testing machine limitations, defect location, and stress redistribution mechanisms in determining the fatigue behavior of specimens with induced defects.

Conclusions and Future Work

This study demonstrated the impact of engineered defects on the fatigue behavior of AM-SFTs through IRT and fatigue limit estimation. Both pristine and engineered defect configurations were considered, with cyclic step-loading applied during the fatigue tests on each specimen. The results showed that while defects were expected to act as stress concentrators and reduce fatigue limits, the observed fatigue threshold for the defected specimen did not decrease as anticipated. This suggests that the chosen defect did not drastically affect the overall fatigue performance under the tested conditions.

Future work will focus on increasing the thickness of the specimen from 16 layers (3.2 mm) to potentially 32 layers (6.4 mm), which will increase the UTS value and ensure that the input loads during step loading remain within the resolution of the testing machine. Additionally, the effects of defect placement will be further explored by assessing the fatigue response of specimens with a 6 mm diameter defect positioned in the third layer. This will provide insights into how defect location influences fatigue life.

By exploring these different configurations, future work will enable a better understanding of the mechanisms behind defect-induced fatigue and help refine the design and manufacturing processes for more reliable AM-SFT components.

References

1. P. Pathak, S. Gururaja, V. Kumar, D. Nuttall, A. Mahmoudi, M. M. Khonsari, and U. Vaidya. Examining infrared thermography based approaches to rapid fatigue characterization of additively manufactured compression molded short fiber thermoplastic composites. Composite Structures, 351:118610, 2025.
2. A. Brasington, C. Sacco, J. Halbritter, R. Wehbe, and R. Harik. Automated fiber placement: A review of history, current technologies, and future paths forward. Composites Part C: Open Access, 6:100182, 2021.
3. C. Colombo, A. Tridello, A. P. Pagnoncelli, C. A. Biffi, J. Fiocchi, A. Tuissi, L. M. Vergani, and D. S. Paolino. Efficient experimental methods for rapid fatigue life estimation of additive manufactured elements. International Journal of Fatigue, 167, Part B:107345, 2023.
4. M. Ivey, G. W. Melenka, J. P. Carey, and C. Ayranci. Characterizing short-fiber-reinforced composites produced using additive manufacturing. Advanced Manufacturing: Polymer & Composites Science, 3(3):81–91, 2017.
5. W. S. de Carvalho, J. Draper, T. Terrazas-Monje, A. Toumpis, A. Galloway, and S. T. Amancio-Filho. Fatigue life as-sessment and fracture mechanisms of additively manufactured metal-fiber reinforced thermoplastic hybrid structures produced via ultrasonic joining. Journal of Materials Research and Technology, 26:5716–5730, 2023.
6. D. Palumbo, R. De Finis, P. G. Demelio, and U. Galietti. A new rapid thermographic method to assess the fatigue limit in gfrp composites. Composites Part B: Engineering, 103:60–67, 2016.

7. Z. Jia, M. L. Pastor, C. Garnier, and X. Gong. Fatigue life determination based on infrared thermographic data for multidirectional (md) cfrp composite laminates. Composite Structures, 319:117202, 2023.
8. Y. Yan, M. L. Pastor, E. Abisset-Chavanne, and X. Gong. Rapid identification of fatigue degradation law of composite material based on ir thermography. Composite Structures, 354:118787, 2025.
9. N. Manoharan, P. Pathak, S. Gururaja, V. Kumar, and U. Vaidya. Rapid fatigue characterization via infrared thermography of am-cm composites. In Springer Nature Switzerland, editor, Challenges in Mechanics of Biological Systems and Materials, Thermomechanics and Infrared Imaging, Time Dependent Materials and Residual Stress, volume 2, pages 53–58. 2023.
10. J. Montesano, Z. Fawaz, and H. Bougherara. Use of infrared thermography to investigate the fatigue behavior of a carbon fiber reinforced polymer composite. Composite Structures, 97:76–83, 2013.